Statistical decision methods in the presence of linear nuisance parameters and despite imaging system heteroscedastic noise: Application to wheel surface inspection

Karim Tout, Rémi Cogranne, Florent Retraint

Available online at www.sciencedirect.com

ScienceDirect

Signal Processing 00 (2017) 1–17

Signal Processing

Statistical Decision Methods in the Presence of Linear Nuisance Parameters and Despite Imaging System Heteroscedastic Noise: Application to Wheel Surface Inspection[☆,☆☆]

Karim Tout, Rémi Cogranne, Florent Retraint

ICD - LM2S - ROSAS - Troyes University of Technology - UMR 6281 CNRS
12, rue Marie Curie - CS 42060 - 10004 Troyes cedex - France

Abstract

This paper proposes a novel method for fully automatic anomaly detection on objects inspected using an imaging system. In order to address the inspection of a wide range of objects and to allow the detection of any anomaly, an original adaptive linear parametric model is proposed; The great flexibility of this adaptive model offers highest accuracy for a wide range of complex surfaces while preserving detection of small defects. In addition, because the proposed original model remains linear it allows the application of the hypothesis testing theory to design a test whose statistical performances are analytically known. Another important novelty of this paper is that it takes into account the specific heteroscedastic noise of imaging systems. Indeed, in such systems, the noise level depends on the pixels' intensity which should be carefully taken into account for providing the proposed test with statistical properties. The proposed detection method is then applied for wheels surface inspection using an imaging system. Due to the nature of the wheels, the different elements are analyzed separately. Numerical results on a large set of real images show both the accuracy of the proposed adaptive model and the sharpness of the ensuing statistical test.

Keywords: Adaptive model, Anomaly detection, Hypothesis testing theory, Computer vision applications, Quality control, Heteroscedastic noise

1. Introduction

During the past decades, automated visual inspection (AVI) systems have been broadly used for the inspection of a wide range of "objects" such as fabrics [1, 2, 3], nuclear fuel rods [4], steel [5, 6, 7, 8] or even food [9] to cite few examples. The main role of a computer-vision system is to provide detailed description of the inspected product, from one or several images, in order to detect and classify the possible occurrence of any type of anomaly. Given a set of product specifications, any observation that deviates more than a prescribed value from what is standard, or normal, is considered as an anomaly. Furthermore, if the anomaly surpasses certain acceptance limits, which are usually defined by the customer, it is then referred to as a defect.

In general, the anomaly detection process is a –fully or partially– manual process conducted by operators, whose main role is to inspect each and every product manufactured along

[☆]This work has been done within project VISION supported by the Conseil Rgional de Champagne-Ardenne under industrial collaborative project framework, Grant E201314628.

Email address: remi.cogranne@utt.fr (Rémi Cogranne)
URL: http://lm2s.utt.fr/fr/membres/cogrannr.html ; personal webpage: http://remi.cogranne.pagesperso-orange.fr/ (Rémi Cogranne)

the fabrication line. A single operator might have to inspect thousands of manufactured products during the day. As a result, this manual process is usually subjective, labor intensive, and sometimes biased. Therefore, and in order to overcome these difficulties, there is a great need for fully automatic systems that are fast and sufficiently efficient, and which are used to replace, or to assist, the operators to control the presence of defects [10]. Such systems have to be reliable, and trustworthy, for the detection of various types of defects. However, depending on inspected objects geometry and their internal structure, the detection may be made difficult due to the non-anomalous "background".

1.1. State of the Art

Prior methods for surface anomaly detection based upon images captured with an AVI system can be divided into three categories [1, 4, 11]: 1) Generic methods that are highly flexible as they are not based on any prior knowledge on inspected objects [5], 2) Specific methods that are based on ground truth or examples of a reference [11], and 3) Methods based on computer vision and image processing, see [12, Chap. 15] , that usually require prior information on the non-anomalous object.

The first category includes anomaly detection methods that do not require any prior model of object's structure. Different types of filters [3, 6], such as median filter or Gaussian filter, morphological operations [13], and histogram equalization [14], have been all applied for noise reduction, image enhancement, with the aim to improve the contrast between the anomaly and the non-anomalous background. These tools, followed by pattern recognition methods [15, 16] or thresholding operations [7, 8], illustrate the core architecture of this type of methods. First-order gradient filter followed by thresholding is one of the most commonly used approach in this category [6, 8, 17]. More recently, state-of-the-art image processing methods, such as multi-resolution representation [18], sparse dictionary learning [19] and variational methods [20], have all been applied for automatic anomaly detection. Similarly, classification methods have been used for automatic recognition of anomalies, mainly with the help of supervised machine learning [7, 8, 21, 22, 24]. These methods consist of separating the inspected image into regions of distinct statistical behavior [23], based on the assumption that common properties can define all kinds of anomalies and distinguish them from any non-anomalous background. The existence of such properties is doubtful in practice and these methods are thus often sensitive to the object and anomaly geometry and to the presence of noise.

In the second category, the detection methods are based on a ground truth: a reference image of the non-anomalous background used as a model [11, 25]. The detection is thus straightforward as it is usually based on mere differences between the reference and the inspected image. If a significant difference is identified, the inspected image is classified as defective [14, 26]. Usually, the reference image is created by averaging multiple anomaly-free images [27]. In an alternative approach, the reference image is estimated from the inspected image using a filter consisting of several masks [28]. This approach is efficient but is very sensitive to experimental conditions, such as object position, illumination and projection angles. Moreover an accurate ground truth may be difficult to obtain in practice.

Finally, methods from the third category make use of prior statistical information on the non-anomalous object. Two main approaches have been proposed to introduce statistical prior knowledge: Bayesian and non-Bayesian approaches. The Bayesian statistical approach allows the design of efficient and rather simple methods for anomaly detection. However those methods require 1) that the anomaly occurs with known prior probability and, 2) that the non-anomalous object is also random with known a priori distribution. Those requirements limit the application of Bayesian methods.
For a more detailed review on methods for automatic defects detection, the reader is referred to [11, 5, 29, 30].

In the anomaly detection problem considered in the present paper, the non-anomalous background of the inspected surface has no interest in the detection process while it may hide the anomalies and, hence, may prevent their detection. In addition, we do not always have prior distributions to model both the inspected surface and the occurrence of anomalies. In such situations, it is more convenient to represent the expected non-anomalous background as a linear combination of basis functions, and to consider non-Bayesian hypothesis testing methods for anomaly detection.
As a result, the method proposed in present paper belongs to the third category, and, specifically, to non-Bayesian approaches. It is based on some knowledge on the inspected surface and uses it to design a broad method for rejecting the non-anomalous part of this inspected surface. This allows to meet the practical constraints of the industrial process, such as speed and reliability, while using geometric knowledge on the inspected object which is easily available at the manufacturing stage.

1.2. Contribution of This Work

In this paper, it is proposed to design a non-Bayesian method based on an adaptive model of the non-anomalous part of the inspected surface, also referred to as the "background". This original adaptive model is interesting as it allows the inspection of a large range of surfaces, with different geometries, without prior information or Computer-Aided Design (CAD) models of the inspected object; this extends the application of the proposed methodology to various quality inspection domains. In addition, the use of this model with an heteroscedastic statistical noise model of digital images prevents the need to calibrate the imaging system. Eventually, the proposed model is accurate enough to allow the detection of small defects that are hardly visible by naked eyes. The proposed method is then applied for wheels surface inspection to detect "appearance defects" that are located on the surface of the wheel. This specific application allows challenging the efficiency of the proposed methodology in several ways; indeed the surface of the wheel is rather complex to inspect and requires an accurate model, while as in most of industrial applications, the large number of wheels produced every day requires mastering precisely the properties of

the statistical test.
Our prior works [31, 32] also rely on a similar approach for hidden data detection; fundamental differences, however, are that in this paper no information of the potential anomaly (shape, size, position, etc.) is available and that the adaptive model is much more accurate which allows its use in a much wider range of applications.
The main contributions of the present paper are the following:

1. An adaptive statistical model is proposed to represent the imaged surface. This model only requires knowledge of inspected objects geometry making, thus, the anomaly detection system fully automatic and applicable to a wide range of surfaces.
2. The proposed model is accurate, to ensure high detection performance, and computationally simple, for real-time applications.
3. The heteroscedastic noise model is used to accurately describe the noise properties in raw images. Accordingly, for other types of images, the heteroscedastic model can be replaced with the appropriate model without having any effect on the detection accuracy.
4. The statistical properties of the method are explicitly provided. The detection threshold only depends on the false-alarm probability. Consequently, an operator can, for instance, prescribe a false-alarm probability easily and can know which type of anomalies can be detected with which probability.

Numerical results on extended data sets of wheel images from a wide range of wheel types show the relevance of the proposed adaptive statistical model and the sharpness of theoretical established results.

1.3. Organization of This Paper

The present paper is organized as follows. Section 2 states the problem of anomaly detection. Section 3 details the proposed adaptive model of the inspected surface. This model is both simple, for a real-time application, and linear for a simple use within hypothesis testing theory. Section 4 presents the proposed statistical method for anomaly detection. It also establishes the statistical properties of the statistical test. Then, section 5 describes the different elements of the wheel and the approach used for their detection and localization, and presents the preparation of the wheel surface for inspection. Finally, Section 6 presents numerical results and Section 7 concludes the paper.

2. Problem Formulation

Let $\mathbf{Z} = \{z_{m,n}\}$ denote the noisy image, of the inspected surface, of size $M \times N$, where $(m,n) \in \mathcal{Z} = (\{1,\dots,M\} \times \{1,\dots,N\})$. During acquisition, each pixel is corrupted with various noises that change its value from the one expected upon counted photons on the camera sensor. Therefore, each pixel value $z_{m,n}$ at location (m,n) can be represented as:

$$z_{m,n} = \mu_{m,n} + \xi_{m,n} \tag{1}$$

where $\mu_{m,n}$ is the expectation of pixel $z_{m,n}$, or the noise-free value, and $\xi_{m,n}$ represents the noises corrupting the pixel at this location. It is usually assumed that all the noises corrupting the pixel value can be modeled as a Gaussian random variable [40]. A a consequence, the statistical distribution of value for the pixel at location (m,n) is given by:

$$z_{m,n} \sim \mathcal{N}\left(\mu_{m,n}, \sigma^2_{m,n}\right) \tag{2}$$

where $\sigma^2_{m,n}$ is the noise variance. This representation of a pixel is considered when no anomaly is present in the inspected surface. On the contrary, when an anomaly is present in the inspected surface, the expected value of the pixel is affected. Hence, $z_{m,n}$ can be written as:

$$z_{m,n} = \mu_{m,n} + \theta_{m,n} + \xi_{m,n} \tag{3}$$

where $\theta_{m,n}$ is the impact of the anomaly on pixel's expectation. In fact, the anomaly affects a limited area of the image, therefore $\theta_{m,n}$ is equal to zero except for a few pixels in which the anomaly is located. Then, when an anomaly is present, the model of the pixel at location (m,n) becomes:

$$z_{m,n} \sim \mathcal{N}\left(\mu_{m,n} + \theta_{m,n}, \sigma^2_{m,n}\right) \tag{4}$$

When inspecting an image of a surface with the goal of detecting an anomaly, two situations may occur $\mathcal{H}_0 = \{\text{there is no anomaly}\}$ and $\mathcal{H}_1 = \{\text{there is an anomaly}\}$.
From equations (2) and (4), anomaly detection problem can be represented as a decision between the two following hypotheses:

$$\begin{cases} \mathcal{H}_0 : \left\{\mathbf{z}_{m,n} \sim \mathcal{N}(\mu_{m,n}, \sigma^2_{m,n}),\ \forall (m,n) \in \mathcal{Z}\right\} \\ \mathcal{H}_1 : \left\{\mathbf{z}_{m,n} \sim \mathcal{N}(\mu_{m,n} + \theta_{m,n}, \sigma^2_{m,n}),\ \forall (m,n) \in \mathcal{Z}\right\}, \end{cases} \tag{5}$$

with $\theta_{m,n} \neq 0$ for some (m,n).
Formally, a statistical test δ is a mapping $\delta : \mathbb{R}^{M.N} \mapsto \{\mathcal{H}_0; \mathcal{H}_1\}$. When testing two hypotheses, the ultimate goal is to design a Uniformly Most Powerful (UMP) test, which maximizes the power function and satisfies a prescribed constraint on false-alarm probability regardless the anomaly. Let us denote $\mathbb{P}_{\mathcal{H}_i}$ the probability under hypothesis $\mathcal{H}_i$ with $i = \{1,2\}$. The false alarm probability of a test is defined as:

$$\alpha_0(\delta) = \mathbb{P}_{\mathcal{H}_0}(\delta(\mathbf{Z}) = \mathcal{H}_1)$$

Conversely, the power of a test δ is defined as:

$$\beta(\delta) = \mathbb{P}_{\mathcal{H}_1}(\delta(\mathbf{Z}) = \mathcal{H}_1),$$

which also corresponds to $1 - \alpha_1(\delta)$ where $\alpha_1(\delta)$ is the missed-detection probability.

However, resolving such a problem is not straightforward due to various difficulties. In practice, the main difficulty is the presence of unknown nuisance parameters, in the definition of hypotheses, that have no interest for the anomaly detection problem. These nuisance parameters are the pixels' expectation $\mu_{m,n}$ that describe the background, or the non-anomalous part of the inspected surface. Though this nuisance parameter

is not related to the detection problem, it must be carefully taken into account, through the design of a model that accurately describes this background, such that the nuisance parameter does not prevent the detection of anomalies. The model has to be designed with the highest accuracy for distinguishing anomalies from background and, hence, to enhance the detection of the former. However, due to the diversity of inspected surfaces in various applications, this becomes a complex task.
In addition, imaging devices are characterized by an heteroscedastic noise model that makes pixels' variance $\sigma^2_{m,n}$ a function of expectations $\mu_{m,n}$. This property greatly complexifies the removal of the nuisance parameter as well as the design of the ensuing optimal statistical test.
Another difficulty resides in the fact that in this paper, it is considered that no information of the potential anomaly (shape, size, position, etc.) is available. In general, this is the case for many applications. Consequently, as the anomaly cannot be modeled, it is necessary for the background model to be accurate enough to describe the non-anomalous part of the inspected surface, while at the same time avoid the subtraction of the anomaly.

3. Adaptive Parametric Linear Model

3.1. Background Model

For each inspected surface, an original adaptive model is applied to subtract the anomaly-free background. In fact the background, the anomalous-free content of the image that represents the inspected surface, acts here as a nuisance as it has no interest for anomaly detection while it must be carefully taken into account. The present paper proposes to use a parametric linear model to represent the background. Such a model has, indeed, indisputable advantages: it is simple and, hence, usually computationally efficient and can be used within the well-founded statistical theory of invariance to design the anomaly detection method.

Again, let $\mathbf{Z} = \{z_{m,n}\}$ denote the noisy image of size $M \times N$. The inspected area corresponding to image $\mathbf{Z}$ is split into non-overlapping small blocks of size w and h (for width and height respectively). Let us also denote $\mathbf{z}_k$ the k-th block of the inspected image $\mathbf{Z}$; though this block can be seen as a matrix of pixels, it is represented as a vector for the application of the proposed method, typically the pixels are read lexicographically.
The linear parametric model used in this paper is based on the following model for the block $\mathbf{z}_k$, when no anomaly is present:

$$\mathbf{z}_k \sim \mathcal{N}(\mathbf{H}\mathbf{d}_k, \mathbf{\Sigma}_k). \tag{6}$$

Here $\mathcal{N}$ represents the Gaussian distribution thus the model (6) belongs to the very usual one that represents a block $\mathbf{z}_k$ as a sum of non-anomalous content corrupted with additive Gaussian noise. However, the present paper uses an original model for the content, non-anomalous part, and uses a more realistic model for the noise than the Additive White Gaussian Noise (AWGN) that models all the pixels as realization of independent and identically distributed (i.i.d) random variables. The model of the noise is presented in detail in the next subsection.

The linear parametric model is an obvious model (6) to represent the content. It essentially consists in representing all the pixels of the block $\mathbf{z}_k$ as a weighted sum of basis vectors that represent the columns of the matrix $\mathbf{H}$. The weight of this sum represents the vector of parameters $\mathbf{d}_k$. In this paper the model of $\mathbf{H}$ is based on the following two dimensional algebraic polynomial:

$$f(x, y) = \sum_{i=0}^{d_x} \sum_{j=0}^{d_y} c_{i,j} x^i y^j \tag{7}$$

with d_x and d_y the degrees of the polynomial on x and y respectively.
Over the block $\mathbf{z}_k$ the (discrete) coordinates can also be put into vector form, denoted as $\mathbf{x}$ and $\mathbf{y}$ the coefficients $c_{i,j}$ of the polynomial (7) can also be put into a vector $\mathbf{c}_k$ of size $(d_x + 1) \times (d_y + 1)$. Denoting as a matrix $\mathbf{F}$ the polynomial model:

$$\mathbf{F} = (\mathbf{1}, \mathbf{x}, \mathbf{y}, \mathbf{xy}, \ldots \mathbf{x}^{d_x}\mathbf{y}^{d_y}),$$

the model of the background (7) can be written as:

$$\mathbb{E}[\mathbf{z}_k] = \mathbf{F}\mathbf{c}_k, \tag{8}$$

where $\mathbb{E}$ represents the expectation.

The model (6) - (8) is simple and efficient enough for several applications, see [36, 37, 38, 39] for examples in modeling of Internet traffic and image processing. However, for other applications, as the one of wheel inspection presented in this paper, the non-anomalous background is much too complex to be represented with a simple model that remains the same for all the blocks. In fact, a trade-off must be found to keep the degrees of the polynomial (7) as small as possible, for improving ensuing detection performance, while representing with the highest accuracy the content, to enhance the detection of anomalies within the residual noise.

This trade-off leads us to the design of an adaptive model, for which the matrix $\mathbf{F}$ does not remain the same but, instead, changes to take into account the specificity of each block. To this purpose, the proposed method actually exploits the shape of the inspected surface to represent the pixels that share similar profiles. The design of an adaptive linear model based on this idea is done using the Principal Component Analysis (PCA). PCA is a powerful tool to identify patterns in data, and highlight their similarities. In fact, the first principal components retain most of the variation present in the data, which can be added to the model (8) to better approximate the background. Indeed, multiple methods for dimensionality reduction, other than the PCA, can be found in the literature. Probably the most robust ones are sparse dictionary learning methods that proved their efficiency, especially in image modeling [55]. However, considering the PCA for our proposed model can be justified by many reasons. First, our proposed model is mainly based on a polynomial model which can be designed to ensure the orthogonality between the model and the defect. Adding the principal components to the model will not affect this orthogonality, which is crucial for the defect detectability as will be discussed later in section 4. On the other hand, sparse dictionary learning methods are much more robust than the PCA, and

thus may incorporate a large portion of the defect in the background model. Second, in this paper, it is proposed to design a background model accurate enough to represent a wide range of surfaces without prior training step. The model is then computed for each inspected surface on the image of the very same surface itself. To this purpose, the PCA can be applied as it can represent the observations without requiring a prior learning dictionary. A final reason can be mentioned is that the PCA provides good results for a rather low computational complexity, compared to other methods in the same category.

Similarly to the model (8) one can approximate the pixels' value from the block $\mathbf{z}_k$ as:

$$\mathbb{E}[\mathbf{z}_k] \approx \mathbf{P}_k \boldsymbol{\alpha}_k. \tag{9}$$

where $\boldsymbol{\alpha}_k \in \mathbb{R}^\ell$ is the vector of weights for the different Principal Components and the size ℓ the number of selected principal components. The Principal components that are added within matrix $\mathbf{P}_k$ are extracted from the inspected image itself. The index k, here, emphasizes that for different blocks the part of the principal components differs.

With the addition of the adaptive part due to the first few components, the proposed model for representing the background, that is the expectation of the block $\mathbf{z}_k$ (6), can be written as :

$$\mathbb{E}[\mathbf{z}_k] = \mathbf{H}_k \mathbf{d}_k. \tag{10}$$

where the matrix $\mathbf{H}_k$ is made of the polynomial basis vector(8), from the matrix $\mathbf{F}$ and the first principal components (9), from the matrix $\mathbf{P}_k$. The matrix $\mathbf{H}_k$ is thus given by the concatenation of those matrices:

$$\mathbf{H}_k = (\mathbf{F}|\mathbf{P}_k).$$

Similarly the weighting $\mathbf{d}_k$ vector represents the contribution of those different basis vectors.

The range of applications for the proposed parametric model is not only limited to surface inspection, but can rather be used for any application that requires a model of the nuisance parameters for their rejection [51]. In particular, parametric models that are based on a polynomial model have been extensively used in image processing applications, such as image compression [52], or image coding [53]. Furthermore, the concept of adding an adaptive part to the model, in order to aid the polynomial part, has also proven its efficiency. It was mainly used in image processing applications to help model the discontinuities and edges in the image, whether for radiographic image inspection [4], or even to detect hidden data in images [32, 36]. As for the particular domain of surface inspection, the proposed adaptive model can be efficiently applied on partially smooth surfaces, with low textures. In practice, the polynomial part is primarily efficient to accurately represent homogeneous surfaces, or smooth surfaces, with little to no texture. Then, adding the principal components will offer a higher flexibility, and will enhance the performances of the model to handle minor surface complexities. Hence, the proposed model can be used for the inspection of a variety of surfaces, including steel surface [5], ceramic tiles' surface [54], glass surface [28], among others that have mostly a low textured surface.

Consequently, the texture of the inspected surface will have a major role in defining $\mathbf{H}_k$. In total, 5 parameters have to be properly tuned to accurately model the background, while ensuring an efficient detection of defects. The choice of these parameters essentially depends, on the one hand, on the level of complexity of the background and its overall shape, and, on the other hand, on both type and size of potential defects

First, the degrees of the polynomial d_x and d_y have to be large enough to accurately model the background. Depending on the level of complexity of the background in each direction, d_x and d_y might be defined differently. The more the complexity in one direction, the larger the value of polynomial degree in that same direction. Furthermore, it is proposed to add an adaptive part to the model, i.e. the principal components, to better approximate the background. This adaptive part has a role to identify common features in the background, or patterns, and model them using the PCA. In this paper, it is proposed to apply the PCA in a single direction, which represents the direction of the main pattern in the background, but indeed it can be applied on various direction simultaneously. Only the first ℓ principal components are added to the model. This number will increase with the complexity of the pattern, which will be defined mainly by the inspected surface shape. As a result, to more accurately model the background, it is preferable to have large values for the three parameters d_x, d_y and ℓ.
However, having larger values for these parameters may result in a large part of defects being modeled within the background. Therefore, when subtracting the background from the original image, a large part of potential defects will also be subtracted. This would reduce the level of detectability of those defects.

Second, the width w and height h of each block mainly depend on the potential defects size in the inspected area. If the defect affects the majority of pixels inside the block, the estimate of the linear model parameters $\mathbf{d}_k$ will be significantly impacted by the presence of the defect. Consequently, a large portion of the defect will be removed with the background subtraction, thus reducing the level of detectability. Therefore, it is important to define the size of the block according to the potential defects size, in a way to ensure that the majority of pixels in the block belong to the background. It is important to note that in most cases, the defect surface is more textured than the background itself. Hence, even if the defect occupies the majority of the block, it may always be detectable to a certain degree. This is due to the fact that the parametric model is designed to represent the background, therefore the more textured surface of the defect will not be well modeled and accordingly a portion of it will remain after the background rejection.
On the other hand, the size of the block has to remain reasonably small such that the parametric model may be able to accurately model the background. Larger blocks include more background data, and thus may require higher polynomial degrees and more principal components to enable the good modeling of the background.

Section 6.6 further discusses the choice of all those parameters, in the case of wheel surface inspection, and presents the methodology used to select the most suitable values upon experimental data.

3.2. Noise Model

The proposed method relies on the image of the inspected surface. However, any image is corrupted during its acquisition by various sources of noise. A usual model of noise corrupting raw images (that are not processed for quality enhancement, compression, etc.) can be obtained by considering the shot noise separately, due to Poissonian process of photo-counting, and the various read-out noises. In fact the former noise has the specificity that its variance depends on the expected number of counted photons. While on the opposite the latter noise has a variance that depends on experimental setup (such as temperature, exposure time, etc.) that is constant for all the pixels.

It is usually assumed that the number of photons counted over each pixel is high, so that the Poissonian process can be approximated as a Gaussian distribution, and that the read-out noise can also be modeled as a Gaussian random-variable [40, 41]. Hence, this gives a model for all the noises corrupting the pixel at location (m, n) that can be written as follows:

$$z_{m,n} \sim \mathcal{N}\left(\mu_{m,n}, \sigma^2_{m,n}\right) \tag{11}$$

where $\mu_{m,n}$ is the expectation of pixels' $z_{m,n}$, represents its the noise-free value, and is the variance of all the noises is given by:

$$\sigma^2_{m,n} = a\,\mu_{m,n} + b. \tag{12}$$

These parameters (a, b) of the heteroscedastic noise model remain the same for all the pixels. Beside they depend on several acquisition parameters, hence parameters (a, b) are also constant for all the images taken with the same acquisition settings. The model of the noise (11) - (12) is well known for being more accurate than the usual AWGN model for raw images and allows us to take into account the variance of each pixel in the ensuing statistical test, to improve its accuracy [41, 42, 43]. Additionally, it is important to note that it is possible to use any other type of images rather than the raw type, provided that the appropriate noise model for that type of images is used [44, 45]. In fact, for many applications, the model of noise corrupting the acquired image may be more complex, in which cases the noise characterization becomes a major problem. Many researches dealt with such cases, for instance by providing flexible approaches to modeling complex noise based on a robust version of the PCA [56, 57]. In all cases, replacing the noise model will only affect the normalization factor in the ensuing statistical test. However, in the present application, obtaining raw images is simple and ensures to keep as much information on the inspected surface as possible; there is, hence, no need to use a more sophisticated model for the noise corrupting such type of images.

An example of the relationship between pixels' expectation and variance is illustrated in Figure 1. This figure shows the variance of pixels as a function of estimated expectation from the same pixels along with the estimated noise variance estimated from the model (12). Those estimates have been obtained from a few RAW images.

In this work, it is supposed that the camera does not change so it can be calibrated easily. It is thus assumed that the noise

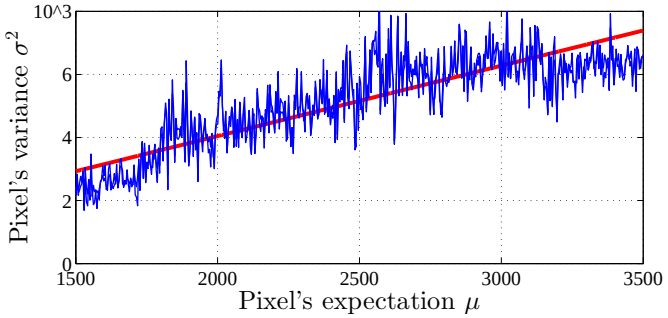

Figure 1: Illustration of the noise model showing, for several images, pixels' variance σ^2 as a function of their expectation μ

model parameters (a, b) are known. The only parameter that has to be estimated, given an image of a surface under inspection, is the expectation of each pixel. However one can note that the noise corrupting the raw images cannot be modeled with i.i.d random variables, the celebrated Maximum Likelihood Estimation (ML) does not coincide with the Least-Square (LS). To tackle this estimation problem without applying a time-consuming optimization algorithm a two-step approach is proposed in this paper. A first estimation is obtained applying the mere LS:

$$\widetilde{\boldsymbol{\mu}}_k^{\text{ls}} = \mathbf{H}_k \left(\mathbf{H}_k^{\mathrm{T}} \mathbf{H}_k\right)^{-1} \mathbf{H}_k^{\mathrm{T}} \mathbf{z}_k.$$

Then, a rough estimation of the noise variance is obtained from $\widetilde{\boldsymbol{\mu}}_k^{\text{ls}}$ by:

$$\widetilde{\boldsymbol{\Sigma}}_k^{\text{ls}} = \mathbf{I}_{w\times h} \times (a\,\widetilde{\boldsymbol{\mu}}_k^{\text{ls}} + b),$$

where $\mathbf{I}_{w\times h}$ denotes identity matrix of size $w \times h$. This rough estimation of the covariance is thus reused to update the estimation of the expectation using the well-known Weighted Least-Square (WLS) given by:

$$\begin{cases} \widetilde{\boldsymbol{\mu}}_k = \mathbf{H}_k \left(\mathbf{H}_k^{\mathrm{T}} \widetilde{\boldsymbol{\Sigma}}_k^{\text{ls}^{-1}} \mathbf{H}_k\right)^{-1} \mathbf{H}_k^{\mathrm{T}} \widetilde{\boldsymbol{\Sigma}}_k^{\text{ls}^{-1}} \mathbf{z}_k, \\ \widetilde{\boldsymbol{\Sigma}}_k = \mathbf{I}_{w\times h} \times (a\,\widetilde{\boldsymbol{\mu}}_k + b). \end{cases} \tag{13}$$

It is, of course, possible to continue this procedure. It has been observed that this two-step method is a good trade-off between accuracy and computational time.

4. Statistical detection of anomalies

When inspecting an image of a surface with the goal of detecting an anomaly, two situations may occur $\mathcal{H}_0$ = {there is no anomaly} and $\mathcal{H}_1$ = {there is an anomaly}. As described above, see Eq. (6), when there is no anomaly, any block of the image can be modeled as $\mathbf{z}_k \sim \mathcal{N}(\mathbf{H}_k\mathbf{d}_k, \boldsymbol{\Sigma}_k)$. On the opposite, when an anomaly is present on the surface, any block can be modeled as $\mathbf{z}_k \sim \mathcal{N}(\mathbf{H}_k\mathbf{d}_k + \boldsymbol{\theta}_k, \boldsymbol{\Sigma}_k)$. Here $\boldsymbol{\theta}_k$ represents the impact of the anomaly on pixels expectation. As described above, the anomaly affects a limited area of the image, therefore $\boldsymbol{\theta}_k$ is equal to zero except in a few blocks on which the anomaly is located. Note that in this paper we consider that the presence of the anomaly has no effect on the variance.

Hence the goal of anomaly detection problem studied in the present paper is to decide between these two following composite hypotheses:

$$\begin{cases} \mathcal{H}_0 : \{\mathbf{z}_k \sim \mathcal{N}(\mathbf{H}_k\mathbf{d}_k, \mathbf{\Sigma}_k)\,,\ \forall k \in \{1,\dots,K\}\} \\ \mathcal{H}_1 : \{\mathbf{z}_k \sim \mathcal{N}(\mathbf{H}_k\mathbf{d}_k + \boldsymbol{\theta}_k, \mathbf{\Sigma}_k)\,,\ \forall k \in \{1,\dots,K\}\}\,, \end{cases} \tag{14}$$

with of course, $\boldsymbol{\theta}_k \neq 0$ for some k.

Formally, a statistical test δ is a mapping $\delta : \mathbb{R}^{w.h} \mapsto \{\mathcal{H}_0; \mathcal{H}_1\}$. The false alarm probability of a test is defined as:

$$\alpha_0(\delta) = \mathbb{P}_{\mathcal{H}_0}(\delta(\mathbf{Z}) = \mathcal{H}_1)$$

where $\mathbb{P}_{\mathcal{H}_0}$ denotes the probability under hypothesis $\mathcal{H}_0$. Conversely, the power of a test δ is defined as:

$$\beta(\delta; \boldsymbol{\theta}_k) = \mathbb{P}_{\mathcal{H}_1}(\delta(\mathbf{Z}) = \mathcal{H}_1),$$

which also corresponds to $1 - \alpha_1(\delta; \boldsymbol{\theta}_k)$ where α_1 is the missed-detection probability. We note that the power function $\beta(\delta; \boldsymbol{\theta}_k)$ depends, of course, on the anomaly $\boldsymbol{\theta}_k$. When testing composite hypotheses, the ultimate goal is to design a Uniformly Most Powerful (UMP) test, which maximizes the power function and satisfies a prescribed constraint on false-alarm probability regardless the anomaly. However, such a test seldom exists. In this paper it is proposed to apply the invariance principle to remove the nuisance parameters $\mathbf{H}_k\mathbf{d}_k$ and to design a Uniformly Best Constant Power (UBCP) test. Indeed, the expectation under $\mathcal{H}_0$ given by $\mathbf{H}_k\mathbf{d}_k$ has no interest for the testing problem (14) but must be taken into account.

To remove the nuisance parameters using invariance theory [46], the idea is to project the observations $\mathbf{z}_k$ onto the orthogonal complement of the subspace spanned by the columns of $\mathbf{H}_k$. This is achieved by using the projector:

$$\mathbf{P}_{\mathbf{H}_k}^{\perp} = \mathbf{I}_{w\times h} - \left(\mathbf{H}_k \left(\mathbf{H}_k^{\mathrm{T}} \widetilde{\mathbf{\Sigma}}_k^{-1} \mathbf{H}_k\right)^{-1} \mathbf{H}_k^{\mathrm{T}}\right) \widetilde{\mathbf{\Sigma}}_k^{-1}, \tag{15}$$

where the estimated covariance $\widetilde{\mathbf{\Sigma}}_k$ is given using the estimated expectation $\widetilde{\boldsymbol{\mu}}_k$ (13). One can note that the projection of observations $\mathbf{z}_k$ onto $\mathbf{P}_{\mathbf{H}_k}^{\perp}$ corresponds to subtracting from the observation the estimated expectation $\widetilde{\boldsymbol{\mu}}_k$. However, because the variance is not constant over all the pixels, it is necessary to normalize the "residuals" by dividing each residual by its standard deviation. Those normalized residuals can be written as follows:

$$\mathbf{r}_k = \widetilde{\mathbf{\Sigma}}_k^{-1/2} \left(\mathbf{P}_{\mathbf{H}_k}^{\perp} \mathbf{z}_k\right). \tag{16}$$

where $\mathbf{A}^{-1/2}$ represents the "square root" of the matrix $\mathbf{A}$ defined such as $\left(\mathbf{A}^{-1/2} \times \mathbf{A}^{-1/2}\right)^{-1} = \mathbf{A}$.

It is then easy to establish [4, 46, 47] that the norm of the normalized "residuals" $\mathbf{r}_k$ follows the distribution

$$\|\mathbf{r}_k\|_2^2 \sim \begin{cases} \chi^2_{\Upsilon}(0)\,,\ \forall k \in \{1,\dots,K\} & \text{under } \mathcal{H}_0 \\ \chi^2_{\Upsilon}(\varrho_k)\ ,\ \forall k \in \{1,\dots,K\} & \text{under } \mathcal{H}_1, \end{cases} \tag{17}$$

where $\chi^2_{\Upsilon}(\varrho_k)$ denotes the non-central χ-squared distribution with $\Upsilon = w \times h - p$ degrees of freedom, here p denotes the number of columns of $\mathbf{H}_k$, and the non-central parameter ϱ_k under hypothesis $\mathcal{H}_1$ is given by :

$$\varrho_k = \left\| \widetilde{\mathbf{\Sigma}}_k^{-1/2} \mathbf{P}_{\mathbf{H}_k}^{\perp} \boldsymbol{\theta}_k \right\|_2^2. \tag{18}$$

Here ϱ_k denotes the "anomaly-to-noise" ratio [4] and is essential to define how detectable the anomaly is.

Based on the residuals $\mathbf{r}_k$ and their distribution, see Eq. (17), the UBCP test can be written as follows

$$\delta = \begin{cases} \mathcal{H}_0 & \text{if } \|\mathbf{r}_k\|_2^2 \leq \tau \\ \mathcal{H}_1 & \text{if } \|\mathbf{r}_k\|_2^2 > \tau, \end{cases} \tag{19}$$

where, in order to guarantee the false-alarm probability α_0, the decision threshold τ is set as follows:

$$\tau = F^{-1}_{\chi^2_{\Upsilon}}(1 - \alpha_0; 0) \tag{20}$$

where $F_{\chi^2_{\Upsilon}}(x, \varrho_k)$ and $F^{-1}_{\chi^2_{\Upsilon}}(x, \varrho_k)$ resp. represent the non-central χ^2 cumulative distribution function and its inverse with non-centrality parameter ϱ_k.
Similarly the power function of the test is given by:

$$\beta(\delta, \boldsymbol{\theta}_k) = F_{\chi^2_{\Upsilon}}(\tau, \varrho_k). \tag{21}$$

One can note from the previous results, Eq. (20)-(21) two important things. First of all, the threshold τ only depends on the false-alarm probability α_0 and is thus constant for all the blocks. Second, the detectability of the anomaly only depends on the non-centrality parameter ϱ_k (18). More precisely, Eq. (18) shows that ϱ_k is defined as the part of the anomaly $\boldsymbol{\theta}_k$ that lies in the orthogonal complement of the subspace spanned by $\mathbf{H}_k$. Hence, an anomaly $\boldsymbol{\theta}_k$ is detectable if and only if $\mathbf{P}_{\mathbf{H}_k}^{\perp}\boldsymbol{\theta}_k \neq 0$.

To better understand the effects of the rejection of nuisance parameters on the defect detectability, let us consider the simple case where the observations $\mathbf{z}_k \in \mathbb{R}^3$ and $\mathbf{d}_k \in \mathbb{R}$, shown in figure 2. In this case, the nuisance parameter is scalar ($\mathrm{rank}(\mathbf{H}_k) = 1$), and the column space of $\mathbf{H}_k$ is a vector $\mathbf{R}(\mathbf{H}_k)$. Its orthogonal complement $\mathbf{R}(\mathbf{H}_k)^{\perp}$, also referred to as the parity space, is then a plane orthogonal to the vector spanned by $\mathbf{H}_k$, and is depicted in blue in figure 2. When projecting the anomalous observations $\mathbf{z}_k$ onto the parity space, the nuisance parameters will be rejected, and only the projection of the anomaly $\mathbf{P}_{\mathbf{H}_k}^{\perp}\boldsymbol{\theta}_k$ will remain in the residuals. Consequently, the detectability of the anomaly $\boldsymbol{\theta}_k$ will mainly depend on how much of the anomaly is present in the parity space, depicted by the value $\mathbf{P}_{\mathbf{H}_k}^{\perp}\boldsymbol{\theta}_k$.
Then, in this work, it is proposed to normalize remaining residuals by taking into consideration the noise corrupting the image. To this purpose, the more realistic heteroscedastic model of the noise has been used, allowing to establish with highest precision the theoretical statistical properties of the ensuing test. This noise model represents the variance of the noise corrupting the image as a linear combination of the pixel's expectation $\boldsymbol{\mu}_k$. Hence, because the variance is not constant over all the pixels, it is necessary to normalize the residuals by dividing each residual by its standard deviation. This procedure is

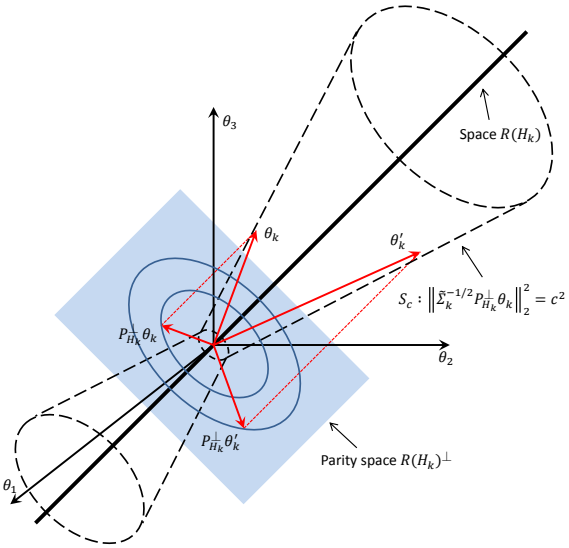

Figure 2: Illustration, in R^3 of observations along with their projections on the parity space $\mathbf{R}(\mathbf{H}_k)^{\perp}$ and a surface of constant power for which "anomaly-to-noise ratio" ϱ_k, see (18) is equal.

illustrated in figure 2. Let us consider two different anomalies $\boldsymbol{\theta}_k$ and $\boldsymbol{\theta}'_k$ that have different projections onto the parity space $\mathbf{P}^{\perp}_{\mathbf{H}_k}\boldsymbol{\theta}_k \neq \mathbf{P}^{\perp}_{\mathbf{H}_k}\boldsymbol{\theta}'_k$. If these two anomalies belong to the same surface $\left\{\boldsymbol{S_c} : \left\|\widetilde{\boldsymbol{\Sigma}}_k^{-1/2}\mathbf{P}^{\perp}_{\mathbf{H}_k}\boldsymbol{\theta}_k\right\|_2^2 = c^2\right\}$ with c a positive constant, this means that they have the same value of non-centrality parameter ϱ_k after normalization, thus have the same level of detectability. Indeed, the surface $\boldsymbol{S_c}$ is defined by the heteroscedastic noise model, and thus it is shaped like a cone with the radius increasing with $\boldsymbol{\mu}_k$.

We have observed that the proposed adaptive model is very efficient in the sense that it represents the background accurately (non-anomalous part of the inspected wheel) while preserving the vast majority of the anomaly within the orthogonal complement.

5. Wheel Inspection Characteristics

The use of AVI systems has been extending to reach various applications. For wheel surface inspection, the detection of "appearance defects" is one of the most challenging tasks that has not been studied yet. "Appearance defects", such as scratches or painting drops, do not have a direct impact on the proper functioning of the wheel, but rather are associated with the aesthetics of the product. These defects are located on the upper surface of the wheel, the one visible to the client. There is a large variety of "appearance defects" that can be classified according to their shape, size, and location on the wheels' surface.

As for the wheels, there are plenty of wheel designs with different shapes and sizes, but they all have some common features and essential elements that characterize a wheel. Based on those elements, it is possible and necessary to define the regions of interest (ROI) on the surface of the wheel, in order to carry out properly the wheel inspection.

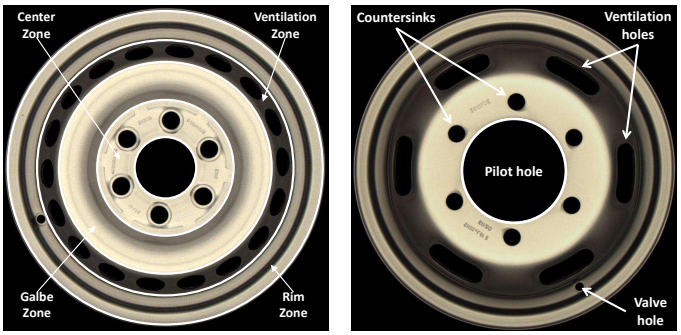

(a) Wheel parts (a) Key elements

Figure 3: Description of the different elements of a wheel

5.1. Region of Interest Extraction

The face of the wheel is a complicated surface to inspect. Each wheel is designed with specific parameters that define its form and geometry. These parameters can be used to split the wheel into different parts (zones), on which the detection method will be applied, see Figure 3(a). Multiple elements can be found in these zones that have to be identified in order not to consider their presence as a defect and, on the opposite, to detect anomalies on those elements. The key elements are the pilot hole, the countersinks, the valve hole and the ventilation holes, see Figure 3(b).

Those elements must be detected and localized prior to the detection of anomalies. Hence, let us first briefly describe how those key elements are detected. Indeed, the position of those elements will be used to perform a geometrical readjustment, which can be considered as a self-calibration.

It is important to note that the parameters describing the geometry of the wheel, and especially the key elements mentioned above, are known because the design of the wheels currently manufactured is also known. The knowledge of those parameters, such as the wheel radius and pilot hole radius, for instance, is useful as it allows to reduce the search area.

First of all, it is needed to detect the center of the wheel that coincides with the center of the pilot hole. The detection of the pilot hole and the localization of its center is carried out using the Circular Hough Transform (CHT). This is one of the most robust and commonly used methods for circular shape detection [33]. In addition, the prior knowledge of the radius makes the CHT computationally very efficient as the only two unknown parameters are the coordinates (x_0, y_0) of the center of the pilot hole. An example of the application of CHT for the pilot hole detection and localization of its center is presented in Figure 4.

Once the Pilot hole is located, the countersinks and the valve hole can be detected. Once again, knowing the distance from the wheel center to the countersinks and the valve hole helps reduce the search area along with the computational complexity. The countersinks and the valve hole are also detected using the CHT. Note that, because on any wheel the valve hole is always either in front of a countersink, Figure 3(a), or between two countersinks, Figure 3(b), the detection of the valve hole is done on a small number of areas that correspond to the known

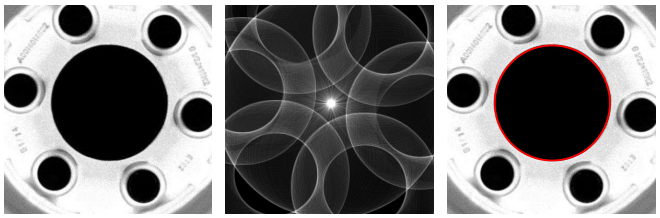

(a) Wheel center (b) CHT result (c) Hole Detection

Figure 4: Illustration of steps for pilot hole detection

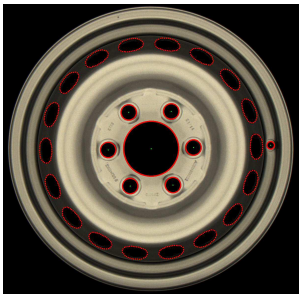

Figure 5: Detection result

distance from the pilot hole center.
The last and most complicated step is the detection of the ventilation holes. Those elements may exhibit a wide range of different designs for aesthetic reasons but also in order to reduce the weight of the wheel with minimal structural impact. This high variety in shape of the ventilation holes explains the choice of the active contour models, or Snakes, for their detection [34, 35]. Such models have been extensively used in image segmentation in order to detect complex geometrical forms. The final result of the detection procedure to locate all those elements is shown in Figure 5.

Once the pilot hole, countersinks, valve hole and ventilation holes are detected and located, one can split the wheel within several areas, see Figure 3(a), which are all inspected separately. Note that, though not very original, the detection of those elements has to be extremely robust as any error will lead to a false alarm of the anomaly detection method. To give an idea, the number of wheels produced over one year is about 4 million wheels, and yet, not a single error has been observed in those key elements location.

5.2. Data Preparation

AVI systems for anomaly detection have been widely used for their efficiency and unbiased results compared to human inspection. But, on the other hand, one great drawback in certain cases is that such systems might be time-consuming. Thus the urge to find new solutions that are fast and reliable.

A first solution might be the use of simple and basic processing methods for anomaly detection, such as the gradient filtering for instance. However, such methods usually go short in terms of detection accuracy and precision, thus making them insufficient for the client requirements. Another solution is to use multitasking, or parallel processing. In fact, this approach highly depends on the inspected product, together with other important factors.

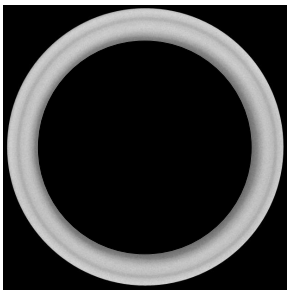

Figure 6: Circular galbe

For wheel inspection, the fact that all the different zones are totally independent from one another, allows us to split the wheel, and apply the detection process in parallel on each zone. Another important advantage in splitting the wheel is that each individual zone has specific characteristics and features, thus specific model parameters. As we can see, all the different zones of the wheel described in figure 3(a) have a circular form. To apply appropriately the detection process, a rectangular image is required. Thus, we proceed by transforming the circular form into a rectangular one.

To explain the data preparation procedure, the galbe zone is considered as an example (see Figure 3(a)).
First, we start by isolating the galbe zone from the rest of the wheel, as illustrated in figure 6. The second step is to unfold the circular area to create a rectangular one. Let us denote $(\mathbf{r_1}, \mathbf{r_2})$ the lowest and highest radius of the galbe area respectively. Normally, a circle of radius $\mathbf{r}$ has a perimeter of $2\boldsymbol{\pi}\mathbf{r}$. As $\mathbf{r_2} > \mathbf{r_1}$, hence $2\boldsymbol{\pi}\mathbf{r_2} > 2\boldsymbol{\pi}\mathbf{r_1}$, the circular area will turn into an isosceles trapezoid with a length ratio of $\mathbf{r_2}/\mathbf{r_1}$. In fact, to get a rectangle, either you define the length as $2\boldsymbol{\pi}\mathbf{r_1}$, thus you lose some pixels, or you define it as $2\boldsymbol{\pi}\mathbf{r_2}$ and you add the missing pixels to complete the form. For the purpose of not losing any information, it is clearly best to define the length of the resulting matrix as $2\boldsymbol{\pi}\mathbf{r_2}$ and add the missing pixels by duplicating its neighbors. It is worth noting that the number of missing pixels is proportional to the ratio $\mathbf{r_2}/\mathbf{r_1}$, which is in our case less than 1.5 for all the different types of wheels.

As a result, to unfold the circular galbe properly, the resulting rectangular matrix must be of height $\mathbf{r_2} - \mathbf{r_1} + 1$ and of length $2\boldsymbol{\pi}\mathbf{r_2}$. In fact, the unfolding procedure can be represented as a transition from the Polar coordinate system to the Cartesian coordinate system. Let us denote $(\mathbf{x_c}, \mathbf{y_c})$ the coordinates of the center of the wheel. Each pixel of the galbe in the Polar coordinate system is represented by its radius $\mathbf{r}$ and its angle $\boldsymbol{\theta}$. The transition system can be represented as :

$$\begin{cases} \mathbf{x} = \mathbf{x_c} + \mathbf{r} * cos(\boldsymbol{\theta}) \\ \mathbf{y} = \mathbf{y_c} + \mathbf{r} * sin(\boldsymbol{\theta}) \end{cases} \tag{22}$$

where $(\mathbf{x}, \mathbf{y})$ are the Cartesian coordinates of the correspondent Polar coordinates $(\mathbf{r}, \boldsymbol{\theta})$. Figure 7 represents the resulting unfolded galbe to be inspected.

Figure 7: Typical example of the unfolded galbe of a wheel.

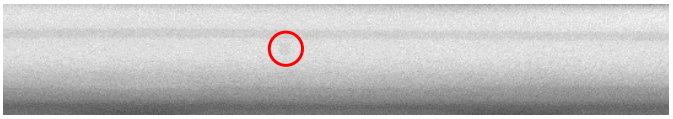

Figure 8: Example of a typical defect that it is wished to detect

6. Experiments and results

6.1. Common core of all experiments

All the images used in this paper are raw images (*i.e.* without any processing operation) using an area scan camera installed over the production line of a wheel factory that produces around 20 000 wheels per day. The acquired raw images are made of 2046×2046 pixels of 12 bits depth ; in most of the experiments presented in this paper, only the red channel is used for simplicity and clarity.

Regarding to the adaptive part of the background model, as mentioned in the section 3.1, it is beneficial to use the shape of the inspected surface to better design this part of the model. Due to the circular shape of the wheel, we applied the PCA by considering the columns of the unfolded image as different observations. Hence, the columns of $\mathbf{P}_k$ in equation (9) represent the part of the first principal components, computed for each inspected wheel on the image of the very same wheel itself, that corresponds to the location along the rows of the extracted block $\mathbf{z}_k$ and reshaped such that it is constant along the rows.

Then, in order to estimate accurately the heteroscedastic noise model parameters (a, b), a batch of raw images of test pattern has been used. As mentioned previously, these parameters (a, b) only depend on acquisition parameters. All the different types of wheels considered in this paper are acquired using the same camera settings; the parameters (a, b) are, thus, constant for all the images. Using the method proposed in [42] for the estimation of parameters (a, b) from the noise model resulted in $a = 2.23$ and $b = -420$.

Finally, to gain a better perspective on the average size of the defects in the wheel image, it is worth noting that each millimeter of the wheel surface corresponds to about 2 pixels in the wheel image. This ratio is a rough average over all the manufactured wheel types as it depends on the wheels height and on the camera settings.

The rest of this section is divided into four parts. In the first part, the advantages of adding the adaptive part, based on the PCA, in the proposed model of the background are proven. The second part investigates the advantages of using the heteroscedastic noise model rather than the usual AWGN model. The third part is aimed at studying the performance and accuracy of the proposed adaptive model of the background. And finally, the fourth and last part compares the performance obtained using the proposed detection method with performance from other recently proposed surface defect detection methods. Note that the first two parts of this section can also be considered as a comparison between the proposed method and other parametric methods that neither contain adaptive parts within linear model, nor take into account accurate imaging system heteroscedastic noise model.

6.2. Improvement of Detection Accuracy Due to the Model Adaptivity

Figure 8 presents an example of the galbe zone, with a typical defect that represents the lower limit of the detection criteria, above which the defect is intended to be detected. It has a circular form which can be considered to simulate various types of real defects. Note that the defect is highlighted with a red circle as it is rather difficult to see from naked eyes. This defect is used in the first and third part of the experiments.

In the first part of the experiments, the goal is to investigate the advantages of adding the adaptive part, in other words, the Principal Components, to the proposed background model. To this purpose, it is needed to compare the performance of the proposed model in two different scenarios, where in the first scenario the background model consists of the polynomial part and the adaptive part, and in the second scenario the background model only consists of the polynomial part.

The defect in Figure 8, has been used to perform a Monte-Carlo simulation on 3 000 images. Because it is hardly possible to obtain many images with similar defects, we picked randomly a set of 3 000 non-anomalous images on which the defect has been superimposed. In fact, it is rather difficult to obtain images with defects, while images of wheels without any defect are easy to obtain. The proposed model parameters have to be adjusted in a way to highlight the effect of the adaptive part. As the Principal Components are used to assist the polynomial function to better model the complexity of the wheel along the rows, it is then possible to increase the block height and study the performance. Therefore the block is set to a size of $h = 40$ (height) and $w = 40$ (width).

Figure 9 and Figure 10 compare the mean power value of the statistical test performed on the 3 000 images, in the two-case scenarios mentioned above, for different values of the defect intensity and defect radius respectively. In Figure 9 the defect radius is set to 5, and in Figure 10 the defect intensity is set to 150. In both cases, the false-alarm probability is set to 0.01.

In the two figures, the blue plots have been obtained using the proposed adaptive model with the degrees of the polynomial set to $d_y = 5$ (along the height) and $d_x = 2$ (along the width) and the number of Principal Components added to this model is $\ell = 3$ giving us a total of $p = 21$ parameters, which is very small compared to the number of pixels (1600). As for the red plots, they have been obtained using the same polynomial degrees, but without any Principal Components added.

As it can be clearly seen in the two Figures, the model with Principal Components added outperforms the model without any Principal Components added in terms of detection power. For a defect radius of 5 and a defect intensity of 150, the detection power values can be read from both figures. If no Principal Components are added, the detection power only reaches a

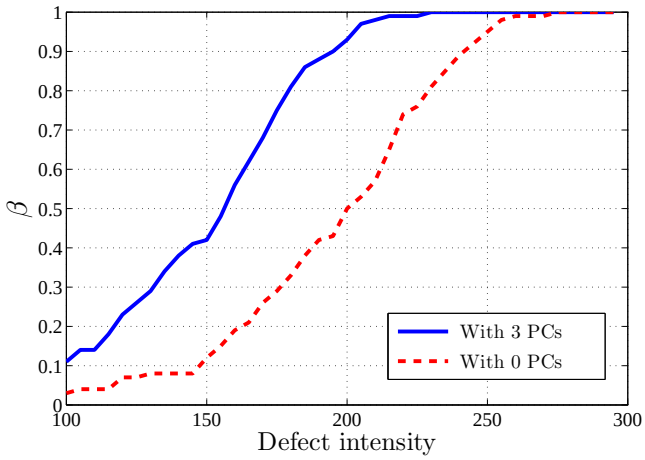

Figure 9: Real power curves with $\ell = 3$ PCs and $\ell = 0$ PCs function of the defect intensity with a fixed defect radius = 5

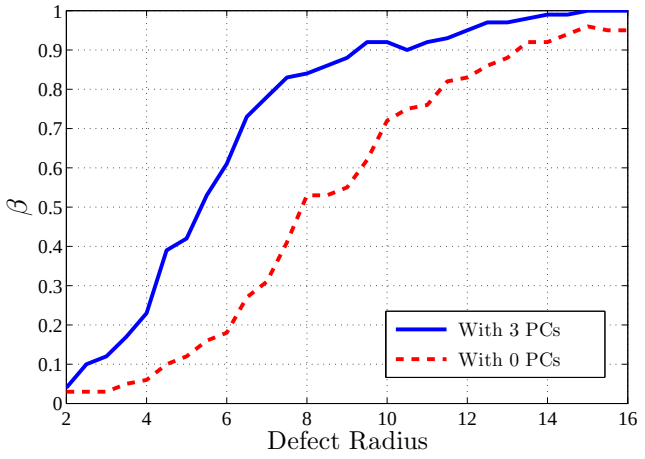

Figure 10: Real power curves with $\ell = 3$ PCs and $\ell = 0$ PCs function of the defect radius with a fixed defect intensity = 150

value of 0.12. By adding 3 Principal Components to the model, the detection power increases to a value of 0.42, which is almost 4 times higher than the previous case. One can also notice from Figures 9 and 10 that the two plots converge to a nearby value of 1 with the increase of the defect intensity or radius.

6.3. *Improvement of Detection Accuracy Due to Heteroscedastic Noise Model*

In this section it is aimed to highlight the advantages of using the heteroscedastic noise model rather than the usual AWGN model. As mentioned in subsection 3.2, the heteroscedastic noise model expresses the relationship between pixels variance σ^2 and their expectation μ as a linear polynomial. As for the AWGN model, the variance σ^2 is considered constant all over the image, independent from pixels expectation.

To investigate the choice of the noise model, it is necessary to study the effect of pixels' expectation on the normalization process. In fact, the noise model that one uses defines the covariance matrix which has a primary role to normalize the residuals norm. From (17), the empirical distribution of the normalized residuals norm must follow a central χ-squared distribution with $\Upsilon = w \times h - p$ degree of freedom. Any inaccurate normalization will have a direct effect on the centrality of the non-anomalous normalized residuals norm.

Figure 11: Block 1 and Block 2

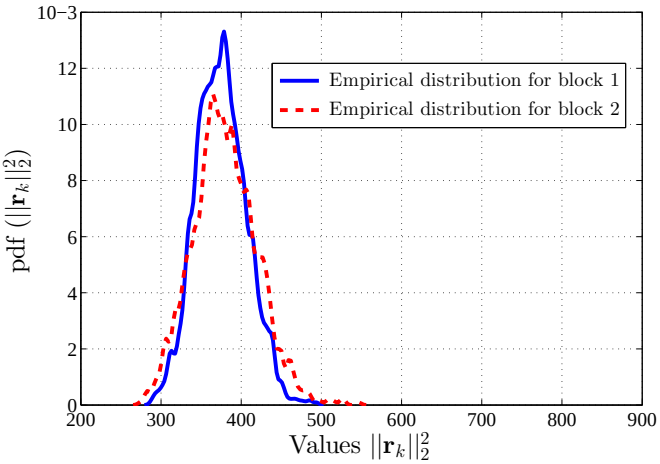

Figure 12: Empirical distributions of normalized residuals norm over block 1 and block 2 using the heteroscedastic noise model

Figure 11 represents two blocks within two different regions of the galbe zone. As one can notice, the block 1 is located on a bright region of the galbe zone, with high pixels' expectation values. As for the block 2, it is located on a darker region of the galbe zone, which means lower values of pixels' expectation. It is important to note that Block 1 and Block 2 do not contain any type of defect.

Those two blocks are used to perform a Monte-Carlo simulation on 3 000 non-anomalous images using the proposed adaptive model, the first time with the heteroscedastic noise model, and the second time with the usual AWGN model.

Figure 12 represents the empirical distributions of normalized residuals norm $\|\mathbf{r}_k\|_2^2$ for Block 1 and Block 2 using the heteroscedastic noise model. The two distributions are centered around the same value of $w \times h - p = 20 \times 20 - 21$, which indicates that the normalization is adapted to the pixels expectation variation.

On the other hand, Figure 13 represents the empirical distributions of the normalized residuals norm $\|\mathbf{r}_k\|_2^2$ for Block 1 and Block 2 using the AWGN model. We observe that the empirical distribution for Block 1, which has high values of pixels expectation, is shifted to the right, while the empirical distribution for Block 2, which has low values of pixels expectation, is shifted to the left.

This result can be explained by the model from Equation (12). By using the AWGN model, the normalization of the residuals norm is independent from pixels' expectation values. As a consequence, the variance is considered constant all over the image. In reality, the relationship between pixels' expec-

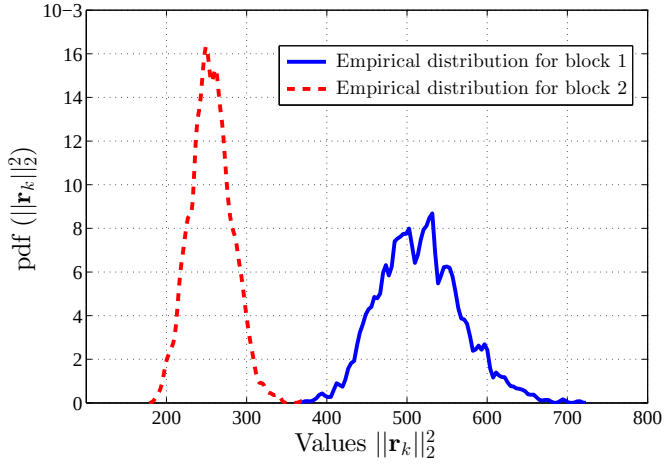

Figure 13: Empirical distributions of normalized residuals norm over block 1 and block 2 using the AWGN model

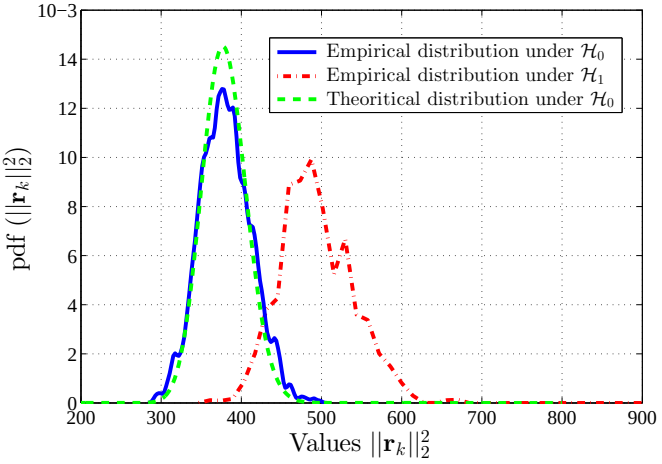

Figure 14: Empirical and theoretical distributions of normalized residuals norm for images with and without defect

tation and variance is a linear polynomial (12) with a positive slope value (see Figure 1), which means that the pixel variance increases with its expectation. For Block 1, having higher pixels' expectation values in reference to the average expectation value, implies higher variance values, which also indicates the need for a higher normalization factor. As for Block 2, it is the other way around; Lower pixels expected values in reference to the average expectation value, implies lower variance values, which also indicates the need for a lower normalization factor.

These results show the efficiency of the heteroscedastic noise model to achieve the appropriate normalization of the residuals norm. In conclusion, one can clearly state that, in case of dealing with raw images, the AWGN model is not efficient, and that the use of the heteroscedastic noise model is crucial to achieve the perfect normalization results.

6.4. *Comparison Between Empirical and Theoretically Established Results*

In the third part of the experiments, it is wished to show the relevance of the proposed statistical test and the accuracy of the theoretical results. Once more a Monte-Carlo simulation has been performed on 3 000 images with and without the presence of the defect shown in Figure 8. This defect has an intensity of 200 and a radius of 5.

Figure 14 presents the empirical distribution of normalized residuals norm $||\mathbf{r}_k||_2^2$ on which the proposed test is based, see Eq. (19). It has been obtained using the proposed adaptive model over blocks with size $h = 20$ (height) and $w = 20$ (width). Note that for this experiment, the size of the block has been reduced to more precisely model the background. The degrees of the polynomial used are $d_y = 5$ (along the height) and $d_x = 2$ (along the width) and the number of Principal Components added to this model is $\ell = 3$.
The gap between the empirical distribution under $\mathcal{H}_0$ and the empirical distribution under $\mathcal{H}_1$ is due to the non-central parameter ϱ_k under hypothesis $\mathcal{H}_1$ (18). As mentioned above, the defect used in this simulation represents the lower limit of the detection criteria, above which the defect is intended to be detected. With this information in mind, Figure 14 shows that the detection of the defect is possible with certain classification error.

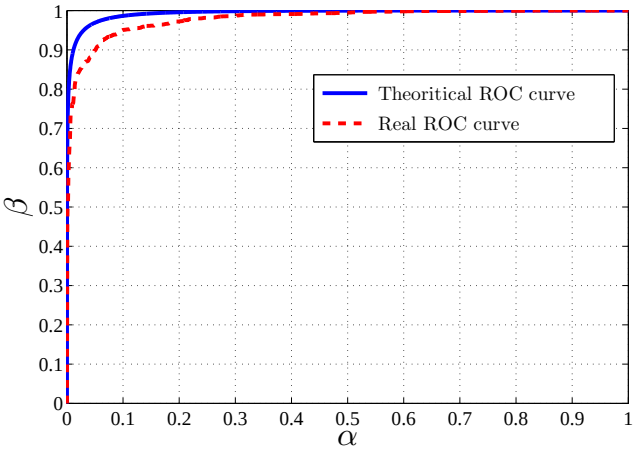

Figure 15: Real and Theoretical ROC Curves

Besides, Figure 14 also compares the empirical distribution under $\mathcal{H}_0$ with the theoretical one (17). A small discrepancy can be observed between the empirical and the theoretical distributions.

The effect of the discrepancy can be illustrated in Figure 15 which represents the real and theoretical ROC curves. As one can notice, the performance of the proposed model is slightly lower than it is expected theoretically.

This can be explained by the two following facts. First, the estimation of pixels expectation is not perfect and has itself a non-negligible variance, which is not yet taken into account in the proposed test. Second, the proposed adaptive model, though efficient, is not perfect and, hence, maybe sometimes unable to describe the background with highest accuracy, putting part of the non-anomalous background among the residuals.

6.5. *Comparison With the State-of-the-art*

Finally, in this last section of numerical results, it is wished to compare the performance of the proposed method with methods recently proposed in the literature for surface defect detection.

To this intent, Monte-Carlo simulations have been performed on 3 000 images with and without the presence of a defect that has the same form as the one shown in Figure 8, but with an intensity of 300 and a radius of 5.

The first simulation has been performed using the proposed adaptive model over blocks with size $h = 20$ (height) and $w = 20$ (width), with the degrees of the polynomial set to $d_y = 5$ and $d_x = 2$ and the number of Principal Components added to this model set to $\ell = 3$.

The second simulation has been performed using the detection method detailed in [48]. It consists of two phases: 1) a global estimation based on the Phase Only Transform (PHOT) method, which considers the defect as an abrupt change in the image regularity, thus removes the regularity by normalizing the image's Fourier Transform by its magnitude. 2) Then a local refinement procedure which locally refines the estimated region based on the distributions of pixel intensities derived from defect and defect-free regions. Two parameters have to be tuned correctly depending on the input image texture and defect size: the Mahalanobis distance which is the threshold value for detection, and the size of the squared patch used in the local refinement step. They are set to 4.0 and 5×5 respectively, as suggested in the paper [48].

The third simulation uses the detection method introduced in [49]. They propose a regularity measure for defect detection in non-textured and homogeneously textured surfaces based on PCA. The method consists of a small neighborhood window that slides over the inspected image and for each window the regularity measure is then derived from the PCA. Again, two parameters have to be properly selected, as they have major effects on the detection performance. First, a control constant K which defines the threshold value for detection. A small value of K will generate false alarms, whereas a large value of K will result in high miss-detection rate. In order to choose the proper value of K, the paper proposes to select the minimum K value that generates no false alarms when applied to a defect-free training sample. For the proposed performance test, the proper value of K is 3. The second parameter to be tuned is the sliding window size. It should be large enough to contain the entire defect area, however, if it is excessively large it may smooth out the defective area and result in miss-detection. The defect implemented in the performance test has a radius of 5, thus the selected window size is 15×15.

Finally, the proposed adaptive method is compared to the detection method presented in [50] which consists of four subsystems: sensing, detection, classification and post-processing. Only the detection step is for interest in this study. It is based on a foreground extraction step using a median filter, and then a multi-zone detection technique, where each image is divided into multiple overlapped squared areas that undergo a thresholding procedure. The most crucial parameter that achieves an efficient defect detection performance is the median filter size. After many tests on defective and defect-free images, it is set to 13×13.

Figure 16 presents the corresponding ROC curves of the four mentioned detection methods. The proposed adaptive method outperforms the detection method based on the regularity measure [49] and the one based on the median filtering [50]. However, compared to the method based on PHOT [48], the ROC curves seem to be indistinguishable. For a better look, a zoomed-in portion of the plot is illustrated on the same figure, with a false-alarm probability ranging between 0 and 0.03, and a detection probability between 0.8 and 1. This subplot shows that the proposed adaptive method performs slightly better than the one based on PHOT. Still, this comparison cannot be considered as conclusive.

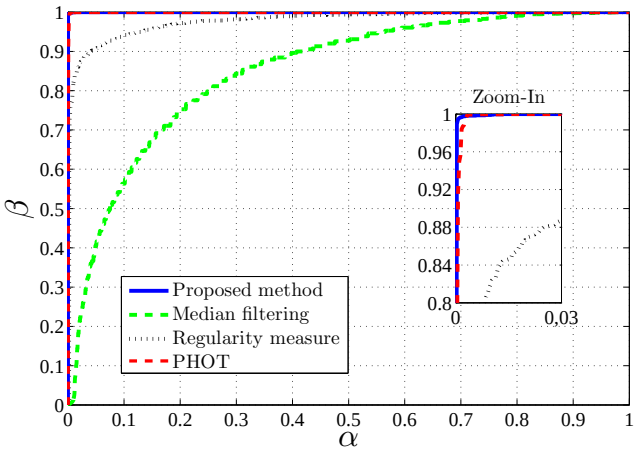

Figure 16: ROC curves of the four detection methods

Therefore, to present a more consistent comparison, it is wished to analyze the effect of the defect radius on the performances of the proposed adaptive method and the one based on PHOT. To this purpose, a similar Monte-Carlo simulation as the one seen in the first part of the experiments is performed, to represent the detection probability value, function of the defect radius, with a defect intensity of 150, and a false-alarm probability of 0.01. The degree of the polynomial used for the proposed adaptive model is $d_y = 5$ and $d_x = 2$ and the number of Principal Components added is $\ell = 3$. Additionally, another goal of this simulation is to show the effect of the block size used in the proposed adaptive model on the detection performance. Hence, three different block sizes have been considered in this simulation.

Figure 17 illustrates the simulation results. The green plot, which corresponds to the method based on PHOT, starts off with the highest detection probability for very small defects with a radius less than 3. It reaches its peak for defects with a radius ranging between 5 and 7. Then the performance starts to decline with the size of the defect. That can be explained in the fact that its detection phase is based on a global method, the PHOT, which must be applied on the whole image at once in order to properly remove the image regularity. Hence, a small defect is seen as an abrupt irregularity while a larger defect becomes slowly considered as a part of the image regularity, and thus partially removed.

As for the proposed adaptive method, it can be noticed that the performance highly depends on the considered block size. For small defects, using a smaller block size leads to a higher detection probability. For a defect radius ranging between 2 and

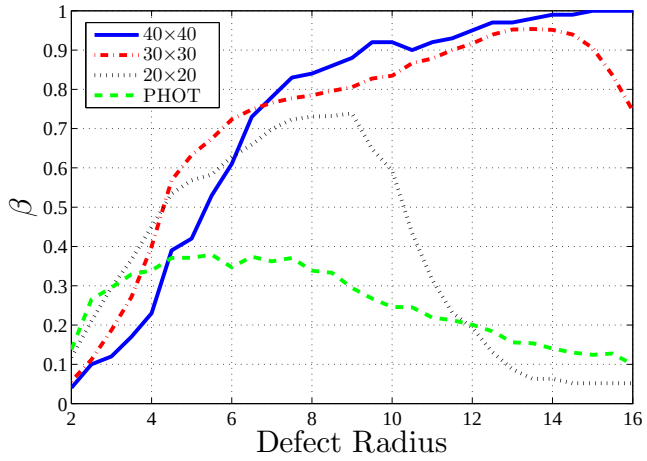

Figure 17: Detection probability function of the defect radius with a fixed defect intensity = 150

4, the proposed adaptive model with a block size of 20×20 is the best choice. For a defect radius ranging between 4 and 7, a block size of 30×30 is more appropriate. And for larger defects, a larger block size of 40×40 becomes the superior choice. That is due to the fact that our method considers that the block is a background image containing a defect, thus the defect occupies a smaller space in the block than the background itself. For a specific block size, the performance of the proposed method continues to rise, with the slope becoming smaller as the defect is becoming larger, till it reaches a certain point when the defect occupies the totality of the block at which the performance drastically declines. This sudden decline in the performance can be observed in Figure 17 for a block size of 20×20 at a defect radius of 9, and for a block size of 30×30 at a defect radius of 14. Therefore, depending on the inspected surface, and on the range on the size of potential defects, one can choose the appropriate block size that gives the best performance.
Finally, this comparison also shows that, for various defect sizes, the proposed adaptive method outperforms the method based on PHOT.

6.6. Real defects

In this section, it is wished to present some results by applying the proposed adaptive model on wheel images containing real defects located on the surface of the wheel. As mentioned above, a number of images with and without defects, have been acquired from a wheel factory that produces around 20 000 wheels per day, among which only a small portion presents a defect.

For each example image with defects, the data preparation procedure presented in Section 5.2 has been applied to obtain the unfolded image of the specific zone of the wheel that contains the defect. Then, the proposed adaptive model has been used to model the unfolded image background and create a model image that ideally does not contain any trace of the defect. Finally, the results are illustrated by a residual image, resulting from the subtraction of the model image from the unfolded image.

Table 1: Proposed Adaptive Model Parameters

Zone	w	h	d_x	d_y	ℓ
Galbe Zone	50	25	2	5	3
Rim Zone	40	15	2	5	5
Ventilation Zone	30	20	2	5	3

Choosing the appropriate parameters for the proposed adaptive model is vital to achieve the best detection results. Each zone of the wheel has its unique features and characteristics, according to which the choice of the proposed adaptive model parameters highly depends. These features and characteristics are not only related to the background homogeneity or pattern, but also to the defect size and shape which dependent much on the specific zone on which the defect is located.

The example images used in this experiment represent numerous types of wheels, with various designs and dimensions, containing defects that are located on various zones of the wheel, as the galbe zone, the rim zone and the ventilation zone. Table 1 lists the proposed adaptive model parameters for each zone of the wheel. The parameters described are the block width w and the block height h, the degrees of the polynomial d_x and d_y, and the number of added Principal Components ℓ.
A detailed, but rather general, discussion on the choice of these parameters has been done in Section 3. In the following, a more in depth explanation of the parameters choice for each zone will be provided, based on the zone texture and potential defect size.

First, it is obvious that, due to the circularity of wheels, in all the different zones pixels share similar values along the horizontal direction, after unfolding process. This characteristic justifies the choice of d_x to a relatively low value of 2 for all the different zones. Along the vertical direction, the texture is much more complex with multiple light reflection artifacts, thus the necessity of higher polynomial degree $d_y = 5$ and the assistance of the Principal Components $\ell = 3$. The Rim zone presents a special case as it contains sharper edges along the rows which explains the use of a higher number of Principal Components ($\ell = 5$) to better model the background.

Regarding the block size, the choice of its width w and height h is mainly related to the defect size, although its height must be always maintained to a low value to help model the complex background along the rows. Briefly speaking, the galbe zone is the largest zone of the wheel, and defects located in this area are usually bigger in size, thus the choice of $w = 50$ and $h = 25$. Defects located on the rim zone, which is the boundary zone of the wheel, are usually medium sized scratches caused by the mishandling of the product, hence the choice of $w = 40$ and a lower value of $h = 15$ due to the special case mentioned above. Finally, defects located on the ventilation zone are usually of small size as they are trapped between the ventilation holes, which explains the choice of $w = 30$ and $h = 20$.

Following this discussion, it is possible to understand the variability of these parameters for the different zones of the wheel. However, to properly determine the exact values of the

model parameters for each zone, it has to be performed by simulations. To this purpose, multiple simulations, with different values of model parameters, have been performed to ensure the best detection efficiency. For each simulation, a different combination of model parameters has been used, with the goal to maximize the detection power β for a fixed value of false alarm α. These simulations were performed in two steps; The first step was defining the size of the block w and h according to the potential defects sizes that could be present on each zone of the wheel. Then, in the next step, multiple combinations of the model parameters d_x, d_y and ℓ were tested to determine the ones that maximize the detection power β for a fixed value of false alarm α with the pre-defined block size.

Figure 18 presents, for a small set of example images, its corresponding unfolded image, model image and residual image, resulting from the use of the proposed adaptive model with the proper parameters corresponding to the zone on which the defect is located.

7. Conclusion

This paper studies the problem of anomaly detection on wheels surface by analyzing digital images captured during the factoring process. The proposed method is based on the detection of wheels elements for analyzing the different zones of a wheel separately. The main originality of the proposed approach is the use of an adaptive linear model for the non-anomalous background. This model is rather simple, very accurate and preserves most of the anomaly within the residuals. Because the proposed model is linear it can be used quite simply within hypothesis testing theory. A statistical test is proposed in this paper for a fully automatic scheme.
Numerical results show the high accuracy of the proposed model and the high performance of the proposed statistical test. The influence of the model parameters will be studied on a wide range of wheels to find the most accurate ones and the variance of the estimations will be taken into account to be able to establish with accuracy the performance of the proposed test.

References

[1] Kumar, A. (2008). Computer-vision-based fabric defect detection: a survey.*Industrial Electronics, IEEE Trans. on*, vol. 55, no. 1, pp. 348–363.

[2] Stojanovic, R., & *al,*. (2001). Real-time vision-based system for textile fabric inspection. *Real-Time Imaging*, vol. 7, no. 6, pp. 507–518.

[3] Zhang, Y., Lu, Z., & Li, J. (2010). Fabric Defect Detection and Classification Using Gabor Filters and Gaussian Mixture Model. *Springer Berlin Heidelberg*, pp. 635–644,.

[4] Cogranne, R. & Retraint, F. (2014, March). Statistical detection of defects in radiographic images using an adaptive parametric model.*Signal Processing*, vol. 96, Part B, pp. 173 – 189.

[5] Neogi, N., Mohanta, D. k., & Dutta, P. K. (2014). Review of vision-based steel surface inspection systems. *EURASIP Journal on Image and Video Processing*, vol. 2014, no. 1, pp. 1–19.

[6] Li, W. B., Lu, C. H., & Zhang, J. C. (2012). A local annular contrast based real-time inspection algorithm for steel bar surface defects. *Applied Surface Science*, vol. 258, no. 16, pp. 6080 – 6086.

[7] Jia, H., & *al,*.(2004). An intelligent real-time vision system for surface defect detection. *17th International Conference on Pattern Recognition (ICPR)*, vol. 3, pp. 239–242.

[8] Naso, D., Turchiano, B., & Pantaleo, P.(2005). A fuzzy-logic based optical sensor for online weld defect-detection. *Industrial Informatics, IEEE Trans. on*, vol. 1, no. 4, pp. 259–273.

[9] Brosnan, T. & Sun, D. W.(2004). Improving quality inspection of food products by computer vision—-a review. *Journal of Food Engineering*, vol. 61, no. 1, pp. 3–16.

[10] Chin, R. T. & Harlow, C. A.(1982). Automated visual inspection: A survey. *Pattern Analysis and Machine Intelligence, IEEE Trans. on*, vol. PAMI-4, no. 6, pp. 557–573.

[11] Mery, D., Jaeger, T., & Filbert, D.(2002). A review of methods for automated recognition of casting defects. *J. Brit. Inst. Non-Destructive Testing*, vol. 44, no. 7, pp. 428–436.

[12] Barrett, H. H. & Myers, K. J.(2013). *Foundations of image science*, John Wiley & Sons.

[13] Anand, R. S. & Kumar, P.(2006). Flaw detection in radiographic weld images using morphological approach. *NDT & E International*, vol. 39, no. 1, pp. 29–33.

[14] Martens, J. B.(1995). Adaptive contrast enhancement through residue-image processing. *Signal Processing*, vol. 44, no. 1, pp. 1–18.

[15] Boerner, H. & Strecker, H.(1988). Automated x-ray inspection of aluminum castings. *Pattern Analysis and Machine Intelligence, IEEE Trans. on*, vol. 10, no. 1, pp. 79–91.

[16] Liao, T. W. & Ni, J.(1996). An automated radiographic NDT system for weld inspection: Part I Weld extraction. *Ndt & E International*, vol. 29, no. 3, pp. 157–162.

[17] Dubovitskiy, D. & Blackledge, J.(2008). A surface inspection machine vision system that includes fractal texture analysis. *International Society for Advanced Science and Technology, Journal of Intelligent Systems*, vol. 3, no. 2, pp. 76–89.

[18] Strickland, R. N. & Hahn, H. I.(1997) Wavelet transform methods for object detection and recovery. *Image Processing, IEEE Trans. on*, vol. 6, no. 5, pp. 724–735.

[19] Liao, H. Y. & Sapiro, G.(2008) Sparse representations for limited data tomography. *5th IEEE International Symposium on Biomedical Imaging: From Nano to Macro*, pp. 1375–1378.

[20] Konukoğlu, R. & Acar, B.(2007). Hdf: Heat diffusion fields for polyp detection in CT colonography. *Signal Processing*, vol. 87, no. 10, pp. 2407 – 2416. Special Section: Total Least Squares and Errors-in-Variables Modelling.

[21] Tan, M., & *al,*.(2016). Weakly Supervised Metric Learning for Traffic Sign Recognition in a LIDAR-Equipped Vehicle. *IEEE Transactions on Intelligent Transportation Systems*, vol. 17, no. 5, pp. 1415–1427.

[22] Yu, J., & *al,*.v(2017). iPrivacy: Image Privacy Protection by Identifying Sensitive Objects via Deep Multi-Task Learning. *IEEE Transactions on Information Forensics and Security*, vol. 12, no. 5, pp. 1005–1016.

[23] Yu, J., Rui, Y. & Tao, D.(2014). Click Prediction for Web Image Reranking Using Multimodal Sparse Coding. *IEEE Transactions on Image Processing*, vol. 23, no. 5, pp. 2019–2032.

[24] Yu, J., & *al,*.(2014). High-Order Distance-Based Multiview Stochastic Learning in Image Classification. *IEEE Transactions on Cybernetics*, vol. 44, no. 12, pp. 2431–2442.

[25] Strecker, H.(1983). A local feature method for the detection of flaws in automated x-ray inspection of castings. *Signal Processing*, vol. 5, no. 5, pp. 423 – 431.

[26] Gonzalez, R. C. & Woods, R. E.(2008) *Digital Image Processing*, Prentice Hall, 3rd edition edition.

[27] Haindl, M. & Mikeš, S.(2004). Model-Based Texture Segmentation. *International Conference Image Analysis and Recognition*, pp. 306–313, Springer Berlin Heidelberg.

[28] Mery, D. & Medina, O.(2004). Automated Visual Inspection of Glass Bottles Using Adapted Median Filtering. *Springer Berlin Heidelberg* pp. 818–825.

[29] Chen, C. H., Pau, L. F., Wang, P. S. P.(2010). *Handbook of pattern recognition and computer vision*, vol. 27, World Scientific.

[30] Koch, C., & *al,*.(2015). A review on computer vision based defect detection and condition assessment of concrete and asphalt civil infrastructure. *Advanced Engineering Informatics*, vol. 29, no. 2, pp. 196 – 210, Infrastructure Computer Vision.

[31] Cogranne, R. & Retraint, F.(2013). An asymptotically uniformly most powerful test for lsb matching detection. *Information Forensics and Security, IEEE Trans. on*, vol. 8, no. 3, pp. 464–476.

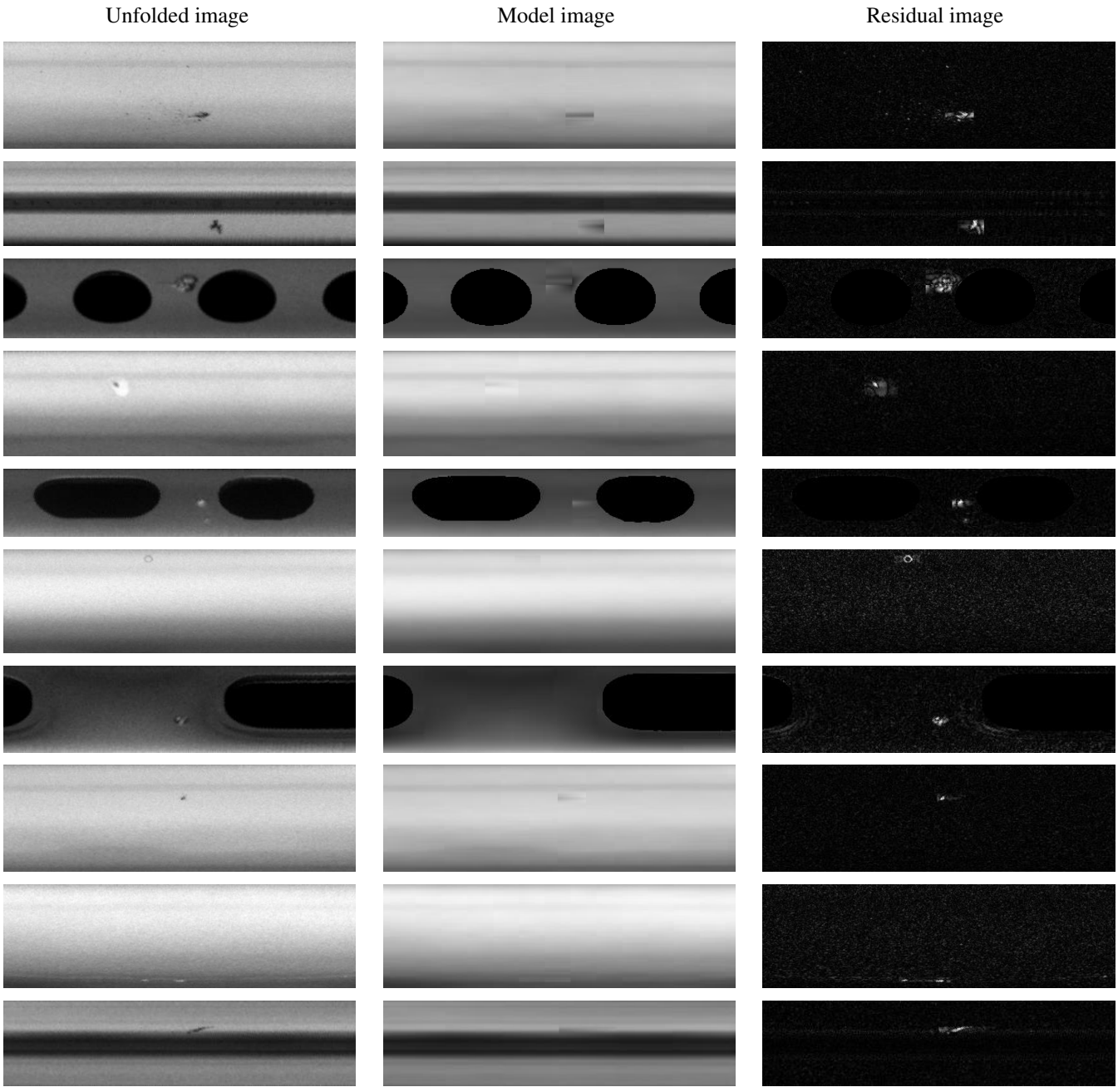

Figure 18: Images of wheels with various defects along with their corresponding model image and residual image

[32] Cogranne, R., & *al,*.(2014). A local adaptive model of natural images for almost optimal detection of hidden data. *Signal Processing*, vol. 100, pp. 169 – 185.

[33] Illingworth, J. & Kittler, J.(1988). A survey of the hough transform. *Computer vision, graphics, and image processing*, vol. 44, no. 1, pp. 87–116.

[34] Kass, M., Witkin, A., & Terzopoulos, D.(1988). Snakes: Active contour models. *International journal of computer vision*, vol. 1, no. 4, pp 321–331.

[35] Lankton, S. & Tannenbaum, A.(2008). Localizing region-based active contours. *Image Processing, IEEE Trans. on*, vol. 17, no. 11, pp. 2029–2039.

[36] Sedighi, V., Cogranne, R., & Fridrich, J.(2016). Content-adaptive steganography by minimizing statistical detectability. *Information Forensics and Security, IEEE Trans. on*, vol. 11, no. 2, pp. 221–234.

[37] Yin, H., & *al,*.(2005). Network traffic prediction based on a new time series model. *Journal of Communication Systems*, vol. 18, no. 8, pp. 711–729.

[38] Nguyen, T. N., & *al,*.(2015). Detection of interest flooding attacks in named data networking using hypothesis testing. *Information Forensics and Security (WIFS), IEEE International Workshop on*, pp. 1–6.

[39] Nguyen, T. N., & *al,*.(2017). Interest Flooding Attack Detection in Real Environment Using Hypothesis Testing. *(submitted)*.

[40] A. Foi, A., & *al,*.(2008). Practical poissonian-gaussian noise modelling and fitting for single-image raw-data. *Image Processing, IEEE Trans. on*, vol. 17, no. 10, pp. 1737–1754.

[41] Thai, T. H., Cogranne, R., & Retraint, F.(2014). Statistical Model of Quantized DCT Coefficients: Application in the Steganalysis of Jsteg Algorithm. *Image Processing, IEEE Trans. on*, vol. 23, no. 5, pp. 1980–1993.

[42] Thai, T. H., Cogranne, R., & Retraint, F.(2014). Camera model identification based on the heteroscedastic noise model. *Image Processing, IEEE Trans. on*, vol. 23, no. 1, pp. 250–263.

[43] Thai, T. H., Retraint, F., & Cogranne, R.(2014). Statistical detection of data hidden in least significant bits of clipped images. *Signal Processing*, vol. 98, pp. 263 – 274.

[44] Thai, T. H., Retraint, F., & Cogranne, R.(2015). Generalized Signal-Dependent Noise Model and Parameter Estimation for Natural Images. *Digital Signal Processing*, vol. 114, pp. 285–297.

[45] Thai, T. H., Retraint, F., & Cogranne, R.(2016). Camera model identification based on the generalized noise model in natural images. *Digital Signal Processing*, vol. 48, pp. 250–263.

[46] Fouladirad, M., Freitag, L., & Nikiforov, I.(2008). Optimal fault detection with nuisance parameters and a general covariance matrix. *International Journal of Adaptive Control and Signal Processing*, vol. 22, no. 5, pp. 431–439.

[47] Cogranne, R. & Retraint, F.(2013). A new tomography model for almost optimal detection of anomalies. *Image Processing (ICIP), Proc. of 20th IEEE International Conference on*, pp. 1461–1465.

[48] Choi, J. & Kim, C.(2012). Unsupervised detection of surface defects: A two-step approach. *19th IEEE International Conference on Image Processing*, Orlando, FL, pp. 1037-1040.

[49] Tsai, D. M., & *al,*.(2012). A fast regularity measure for surface defect detection. *Machine Vision and Applications*, vol. 23, no. 5,pp. 869–886.

[50] Bulnes, F. G., & *al,*.(2016). A Non-Invasive Technique for Online Defect Detection on Steel Strip Surfaces. *Journal of Nondestructive Evaluation*, vol. 35, no. 4, pp. 54.

[51] Basseville, M. & Nikiforov, I.(2002). Fault isolation for diagnosis: Nuisance rejection and multiple hypotheses testing. *Annual Reviews in Control*, vol. 26, no. 2, pp 189–202.

[52] Shukla, R., & *al,*.(2005). Rate-distortion optimized tree-structured compression algorithms for piecewise polynomial images. *IEEE Transactions on Image Processing*, vol. 14, no. 3, pp. 343–359.

[53] Kazinnik, R., Dekel, S. & Dyn, N.(2007). Low Bit-Rate Image Coding Using Adaptive Geometric Piecewise Polynomial Approximation. *IEEE Transactions on Image Processing*, vol. 16, no. 9, pp. 2225–2233.

[54] Hanzaei, S.H., Afshar, & A., Barazandeh, F.(2017). Automatic detection and classification of the ceramic tiles' surface defects, *Pattern Recognition*, vol. 66, pp. 174–189.

[55] Tosic, I. & Frossard, A.(2012). Dictionary Learning. *IEEE Signal Processing Magazine*, vol. 28, no. 2, pp. 27–38.

[56] Wang, Y., Xu, C., Xu, C., & Tao, D.(2017). Beyond RPCA: Flattening Complex Noise in the Frequency Domain. *AAAI Conference on Artificial Intelligence*.

[57] Zhao, Q., Meng, D., Xu, Z., Zuo, W. and Zhang, L.(2014). Robust principal component analysis with complex noise. *International Conference on Machine Learning*, pp. 55–63.